Research Article | Vol. 10, No. 8 / 1 August 2019 / Biomedical Optics Express 4329
Biomedical Optics EXPRESS

Volumetric stimulated Raman scattering imaging of cleared tissues towards three-dimensional chemical histopathology

JUNJIE LI,[1] PENG LIN,[1] YUYING TAN,[2] AND JI-XIN CHENG[1,2,3,*]

[1]Department of Electrical and Computer Engineering, Boston University, 8 St. Mary's St, Boston, MA 02215, USA
[2]Department of Biomedical Engineering, Boston University, 44 Cummington Mall, Boston, MA 02215, USA
[3]Photonics Center, Boston University, 8 St. Mary's St, Boston, MA 02215, USA
[*]jxcheng@bu.edu

Abstract: Thin tissue slice based histology has been used as a gold standard for disease diagnosis since over a hundred years ago. However, histopathological evaluation on two-dimensional slides suffers from large variations due to limited sampling. To improve the diagnostic accuracy, three-dimensional (3D) histology is performed through serial sectioning, staining, imaging and reconstruction of individual slices, which is highly time-consuming and labor intensive. We developed a volumetric stimulated Raman scattering (SRS) imaging method, which provides histology-like information in 3D context without the need for staining with dyes. Using a small molecule clearing agent, formamide, we performed tissue clearing within 30 min and achieved an imaging depth up to 500 μm in highly scattered tissues, including brain, kidney, liver and lung. Through a two-color SRS imaging scheme, we obtained histology-like images in cleared brain tissue slices. Our method has the potential for 3D tissue histopathology to improve the accuracy of histopathological examination.

1. Introduction

Pathological examination has been a gold standard for disease diagnosis and prognosis. Conventional pathology is mostly performed on ultra-thin (4 to 6 μm) tissue slices stained with dyes, such as haematoxylin and eosin (H&E), to enhance structural and intracellular contrast. Pathological examination of stained thin slices is performed under microscope, which provides structural information with single-cell resolution. However, the thin slices lack organizational information of important diagnostic features in three-dimensional (3D) context. Moreover, limited sampling from a bulk of tissues increases the inter- and intra-observer variability [1], reducing the reproducibility and accuracy of two-dimensional (2D) pathology.

Considering these inherent drawbacks of 2D pathology, there has been an increasing demand for 3D histopathology [2]. One straightforward way to obtain 3D pathology is to perform serial-sectioning, staining, imaging and reconstruction. This method is inevitably time-consuming, labor-intensive and destructive to the samples, and thus is not widely adopted in clinical use. To overcome these limitations, other imaging methods are being developed to replace staining-based histology. Optical coherence tomography (OCT) is a microscopic imaging modality with millimeter level penetration depth, yet without chemical selectivity or sufficient resolution (~10 μm) for identifying subcellular features [3,4]. Substantial efforts have been devoted to developing infrared (IR) spectroscopic imaging toward chemical histopathology in the past decade [5–8]. However, this method suffers from relatively low resolution (>2 μm) and limited penetration depth (~30 μm). Although attenuated total reflection IR improves the resolution down to submicron scale, it is only feasible for surface imaging (penetration depth 1-3 μm) [9].

#367541 https://doi.org/10.1364/BOE.10.004329
Journal © 2019 Received 22 May 2019; revised 12 Jul 2019; accepted 22 Jul 2019; published 1 Aug 2019

Biomedical Optics EXPRESS

Recent advances in optical imaging techniques have highlighted other possibilities for histopathology. By taking advantage of the strong absorption of ultraviolet (UV) light (266 nm) by intrinsic molecules, such as DNA and RNA, Wong et al. achieved histology-like imaging of human breast cancer tissues using photoacoustic microscopy with excellent lateral resolution (~330 nm) [10]. Levenson and colleagues developed a microscope with ultraviolet surface excitation (MUSE) for rapid slide-free histology [11]. Glaser et al. deployed light-sheet microscopy for slide-free pathology of clinical specimens with ~200 μm imaging depth [12]. Yet, these methods either suffer from a poor axial resolution (~48 μm) in the case of photoacoustic microscopy or require staining with dyes where the imaging depth is ultimately limited by the penetration depth of dyes.

With intrinsic sectioning capability, nonlinear optical microscopy opens a new window for label-free histopathology. Balu *et al.* demonstrated the use of multiphoton microscopy for rapid examination of human skin tissues [13,14]. Sun and co-workers applied second- and third-harmonic generation (S/THG) microscopies for virtual biopsy of human skin with a penetration depth of ~300 μm. Combination of Coherent anti-Stokes Raman Scattering (CARS), Two-Photon Excitation Fluorescence (TPEF), and SHG/THG microscopies produces H&E staining-like histology images in tissue optical biopsy, as demonstrated by the Popp group [15,16] and the Boppart group [17].

Stimulated Raman scattering (SRS) microscopy is a vibrational chemical imaging modality with submicron resolution and high chemical selectivity [18]. The imaging contrast is from the intrinsic molecules, thus avoids the need for staining with dyes. These characteristics of SRS microscopy fulfills the needs for histological imaging. Application of SRS microscopy for histopathology has been recognized and demonstrated in detection of skin cancer [19] and brain tumor [20–23]. However, due to limited penetration depth (< 50 μm) of SRS imaging in highly scattered tissues, translational use of SRS microscope is restricted to thin tissue sections [24]. Recently, several advances have been made to enable SRS-based volumetric chemical imaging. Utilizing Bessel beams for pump and Stokes, Chen *et al.* reported stimulated Raman projection tomography for volumetric chemical imaging with isotropic spatial resolution [25]. Through tissue clearing by urea, Wei *et al.* achieved volumetric SRS imaging by enhancing penetration depth [26]. However, the urea-based clearing requires days to weeks to complete, thus limiting its potential application in tissue histopathology for clinical diagnosis.

Here, we report a rapid clearing method that enables volumetric SRS imaging with an imaging depth of ~500 μm. By systematically comparing different clearing methods in terms of composition and clearance time, we found that formamide-based clearing method is compatible with SRS imaging at C-H region with minimal background and provides a much faster clearing speed (~30 min) compared to other commonly used methods. We further demonstrate the versatility of this method in various organs, including brain, lung, liver, and kidney. Through two-color SRS imaging, we obtained histology-like images in 3D context of brain tissues, which could potentially improve the diagnostic accuracy of histopathology by conventional 2D sectioning and staining method.

2. Experimental methods

2.1. Stimulated Raman scattering (SRS) imaging setup

Single-color and hyperspectral SRS imaging were performed on a lab-built SRS microscopy system. A femtosecond laser system (InSight DeepSee, Spectra-Physics) operating at 80 MHz was used as the excitation source. The center frequencies of the pump and Stokes beams were tuned to 798 nm and 1040 nm, respectively, to cover the C-H vibrational region. Pulse durations of the pump and Stokes beams are ~120 fs and ~220 fs, respectively. The Stokes beam was modulated by an acousto-optic modulator (1205-C, Isomet) at ~2.3 MHz. Hyperspectral SRS microscopy was achieved on a spectral focusing scheme as described previously [27]. Both femtosecond

Biomedical Optics EXPRESS

pulses were chirped using two 12.7 cm long SF57 glass rods. After glass rods, pulse durations of the pump and Stokes beams were stretched to ~1.3 and ~0.8 ps, respectively. The temporal delay between pump and Stokes pulses was controlled by a motorized translational stage (T-LS28E, Zaber). The power for pump and Stokes beam was set as ~35 mW and ~200 mW (maximal power), respectively, on the sample. A 40X water-immersion objective (NA = 0.8, working distance = 3.3 mm, LUMPLFLN/40XW, Olympus) was used to focus the light on specimen and an oil condenser (NA = 1.4, U-AAC, Olympus) was used to collect the signal in the forward detection scheme. Standard chemicals including Dimethyl Sulfoxide (DMSO) and oleic acid (Sigma) are used to calibrate the Raman shift to the temporal delay.

2.2. Two-color volumetric image acquisition and analysis

To acquire volumetric images, an objective positioner (ND72Z2LAQ, Physik Intrumente) was installed to axially scan the laser foci in the sample with 20 ms settling time at each depth. The maximum display range is ~2 mm in the axial direction. The step interval was set as 4 μm or 1 μm when performing 3D SRS imaging. With a pixel dwell time of 10 μs, the imaging speed is ~1.6 seconds per frame for an image of 400×400 pixels. To achieve two-color SRS images, a lab-built LabVIEW program was designed to control the delay sage moving back and forth between two temporal positions that correspond to Raman shifts at 2850 cm^{-1} and 2930 cm^{-1}. All images were processed and analyzed using ImageJ. The reconstructed 3D images were produced through the 3D plugin in ImageJ.

2.3. Raman spectra measurement

Spontaneous Raman spectra of the clearing solutions were acquired on a confocal Raman microscope (LabRAM HR Evolution, HORIBA). A 532 nm continuous wave laser was used as the excitation light. A 600 lines/mm grating was selected. Spectra in the range from 300 to 3400 cm^{-1} were collected with exposure time of 5 ~ 10 seconds. Raman spectra were processed in Origin software.

2.4. Mouse tissue collection

Balb/c mice (Jackson Laboratory) at ~8 weeks old were used in this study for tissue clearance and imaging. Mice were anesthetized under ~3% isoflurane inhalation. Perfusion was performed with phosphate buffered saline (PBS) buffer and 10% neutral buffered formalin solutions. Organs, including brain, liver, lung, and kidney, were harvested and placed in 10% neutral buffered formalin for overnight or longer time incubation. All animal experiments were conducted following protocols approved by Boston University Institutional Animal Care & Use Committee (IACUC).

2.5. Tissue preparation and clearance

Formalin-fixed tissues were sectioned into slices with 500 ~ 1000 μm thickness using a microtome. Tissue slices were placed in PBS buffer before clearance. Chemicals for tissue clearance, including formamide, sucrose, urea, glycerol, fructose, Triton X-100 and 1-Thioglycerol, were purchased from Sigma. Tissue clearing was performed following previously described procedures [28–31]. For ScaleA2 method, tissue slices were immersed in solution composed of 4M Urea, 10% (w/v) glycerol, and 0.1% Triton X-100 for two days. For sucrose method, tissue slices were immersed in a series of sucrose solutions with gradient concentrations of sucrose at 15%, 30%, 45%, and 60% sucrose plus 2% Triton X-100 with 6 h equilibration time for each step. For ClearT method, tissue slices were immersed in 20%, 40%, 80%, and 95% formamide solutions with 5 min for each step and additional 10 min in 95% formamide solution. Same procedures were followed when the tissue slices were cleared with formamide solution with 5% Triton X-100. Before

Biomedical Optics EXPRESS

imaging, the cleared slices were mounted on glass coverslip with 1% (w/v) agarose gel to prevent sample movement during imaging. Another coverslip was covered on the top the slice.

3. Results

3.1. Comparison of different clearing methods

Tissue clearance has been widely used in fluorescence microscopy for whole tissue imaging and various tissue clearing methods have been developed. Tissue clearing agents improve imaging depth largely by reducing light scattering through multiple mechanisms, including removal of lipids and correction of refractive index mismatch. Based on the clearing agents used, the established tissue clearing methods falls into three categories, organic solvent, aqueous solution and hydrogel [32]. Organic solvents dissolve most of the lipids and create a refractive index matching environment. Aqueous solutions match refractive index mainly through small molecule diffusion. Hydrogel embedding expands the tissue specimen by crosslinking followed by refractive index matching. SRS microscopy at C-H vibrational region will be used for histopathological imaging, as this region produces strongest signal. To avoid the lipid and protein loss from harsh organic solvents and to minimize the background signal from hydrogel, we choose to use high refractive index aqueous solutions composed of small diffusive molecules.

We selected a few commonly used and economically-favorable methods, including Sucrose [31], ScaleA2 [30], and ClearT [29], to test with SRS microscopy. To evaluate the performance of these methods, we sectioned brain tissue into 500 µm thick slices. The clearing solutions were prepared following previous reports [29–31]. Brain slices with the same thickness were immersed into clearing solutions for indicated period. As shown in Table 1, brain slices were immersed in Scale A2 solution for 2 days, in sucrose solutions for 4 days, and in ClearT solutions at gradient concentrations for 30 min in total. After clearing, brain slices were placed together for visual comparison. As shown in Fig. 1(a), compared to PBS immersed group (control), the other three slices all showed increased transparency, while ClearT group showed highest transparency. Then, SRS imaging at 2930 cm^{-1} was performed on these brain slices. A piezo-stage was used to control the imaging depth with an interval of 4 µm. SRS signal diminishes quickly in tissue specimen without clearing as the depth increases and no discernible features can be distinguished at 50 µm depth (Fig. 1(b), Visualization 1). Imaging depth was improved to ~200 µm in ScaleA2 slices (Fig. 1(b), Visualization 2) and ~300 µm in Sucrose slice (Fig. 1(b), Visualization 3). In contrast, recognizable contrast is observed at up to 400 µm depth from the ClearT slices (Fig. 1(b), Visualization 4). Compared to other groups, ClearT slice also shows higher SRS intensity and slower signal decay as the depth increases (Fig. 1(c)). These results suggest that ClearT is compatible with SRS imaging with shorter clearing time and higher imaging depth in tissues.

Table 1. Comparison of different clearing methods in composition and clearance time.

Method	Solutions	Time needed
ScaleA2	4M Urea, 10% (wt/vol) glycerol, 0.1% Triton X-100	> 2 days
Sucrose	15, 30, 45, 60% sucrose + 2% Triton X-100	4 days
ClearT	20%, 40%, 80%, and 95% formamide solutions in PBS (v/v)	30 min

3.2. Versatility in various organs

Besides brain tissues, we also tested the ClearT tissue clearing method in various types of organs, including kidney, liver and lung. Formalin fixed tissues were sectioned into 1000 µm thick tissue slices and cleared using the ClearT method. Tissue slices become visually transparent in ~30 min. Tissue structure and organization are recognizable from SRS images at depth up to 300 µm in cleared kidney (Fig. 2(a), Visualization 5), liver (Fig. 2(a), Visualization 6) and lung tissue slices

Biomedical Optics EXPRESS

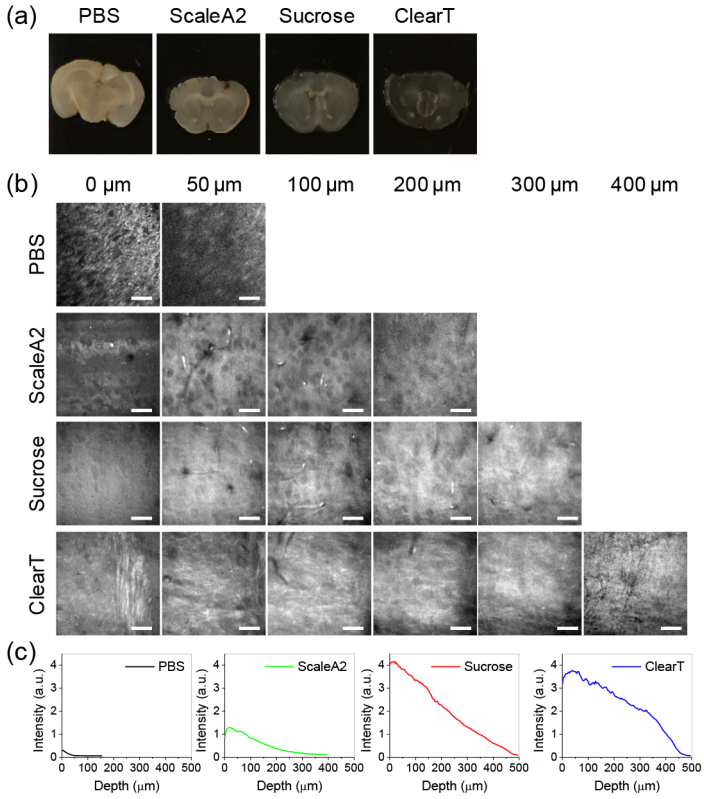

Fig. 1. Comparison of different clearing methods. (a) Pictures of brains slices (~500 μm thick) cleared with different methods. (b) SRS images taken at 2930 cm^{-1} from brain slices cleared by different methods at indicated depth (see Visualization 1–Visualization 4). Nerve fibers and individual cell bodies can be clearly resolved. Image display ranges were adjusted individually to show the contrast clearly. Scale bars: 20 μm. (c) Intensity profile over depth from the images shown in (b).

(Fig. 2(a), Visualization 7). Quantitative analysis of the SRS signal shows faster signal decay in kidney, liver and lung tissue slices (Fig. 2(b)), compared to brain slices, which is likely due to stronger photon absorption by pigments, such as hemoglobin, in these tissues. With decoloring, the imaging depth could be further improved.

3.3. *Spectral measurement of clearing agents*

To understand the sources of SRS signal in the cleared tissue slices, we analyzed the background signal from the clearing solutions through hyperspectral SRS imaging. Compared to PBS, all other clearing solutions show higher SRS signal at 2850 cm^{-1} and 2930 cm^{-1}, with the strongest signal from Sucrose solution (Fig. 3(a)). SRS spectra at the C-H vibrational region from 2800 ~ 3050 cm^{-1} clearly showed higher signal from Sucrose and ClearT solution and relatively lower signal from ScaleA2 solution (Fig. 3(b)). However, Sucrose solution shows much broader spectrum in this region than ClearT solution. ClearT solution has a relatively narrow spectrum with a peak at ~2890 cm^{-1}, suggesting a possibility to minimize its background signal by selecting off-peak Raman shifts. The SRS spectral measurements were confirmed by Raman spectra acquired by spontaneous Raman spectroscopy (Fig. 3(c)). Considering the relative low

Biomedical Optics EXPRESS

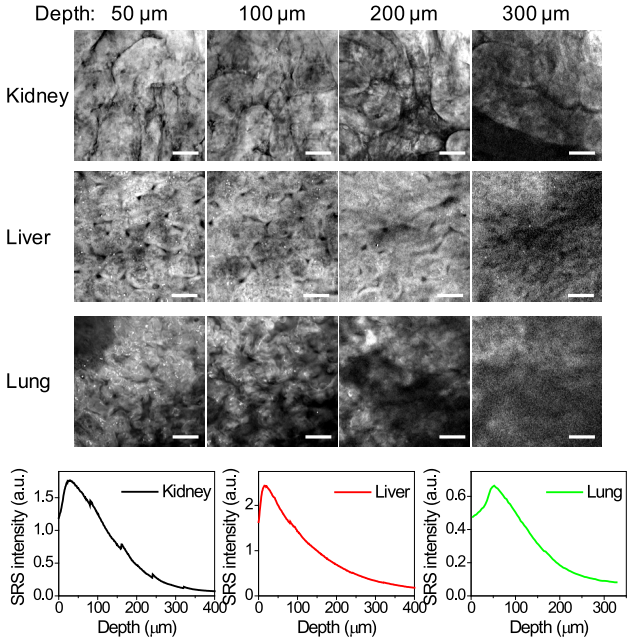

Fig. 2. Demonstration of tissue clearance in various organs. (a) SRS images taken at 2930 cm^{-1} from ClearT cleared kidney, liver and lung tissue slices (~ 1 mm thick) at indicated depth (see Visualization 5–Visualization 7). Tissue organization and characteristic structures like renal tubules (kidney), lobules and veins (liver), and alveoli (lung) can be identified. Image display ranges were adjusted individually to better show the contrast. Scale bars: 20 µm. (b) Intensity profile over depth from the images in (a).

penetration depth from ScaleA2 solution and strong background signal from Sucrose solution, ClearT appears to be the most compatible clearing method for SRS imaging.

3.4. Optimizing the protocol to increase imaging depth

To further improve the imaging depth, we optimized the protocol by adding detergent in the clearing solution. Detergent partially removes the lipids, which cause significant scattering in tissues. Unlike organic solvents, detergents retain the cell morphological integrity. Using detergents is not likely to destruct the structural and morphological information of tissues, which are important features in pathological examination. Using 1000 µm thick brain slices, we compared tissue clearing between ClearT and ClearT with additional 5% Triton X-100. As abovementioned, ClearT provides an imaging depth of ~400 µm with recognizable morphology in SRS images (Fig. 4(a), Visualization 8). With 5% Triton X-100, the imaging depth is enhanced to ~500 µm with resolvable structural information (Fig. 4(a), Visualization 9). With this imaging depth, two cortex layers in the axial direction are clearly revealed (Fig. 4(b), Visualization 10). Use of detergent also enhances the signal intensity compared to ClearT alone (Fig. 4(b)). Nevertheless, supplementation with detergent does not significantly increase the background signal, as indicated by the Raman spectral measurement of the clearing solutions (Fig. 4(c)).

3.5. Two-color histopathological imaging of cleared tissues

To generate histology-like images, we take advantage of chemical selectivity of SRS microscopy. Hyperspectral SRS microscopy can readily separate cellular compartments based on spectral differences, such as nucleus and cytoplasm [33]. However, hyperspectral SRS microscopy takes

Biomedical Optics EXPRESS

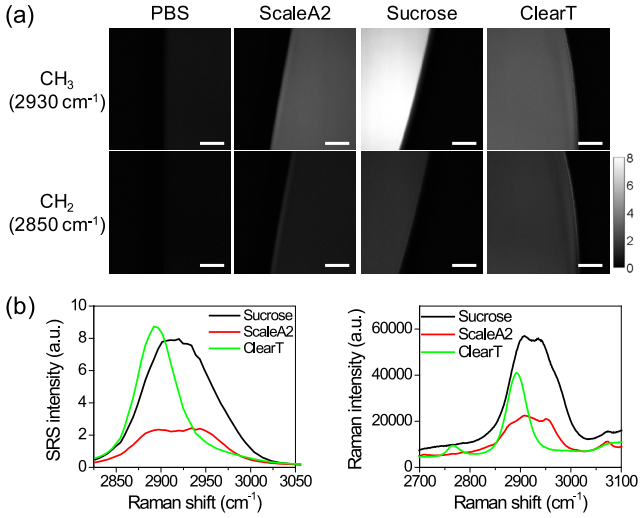

Fig. 3. Spectroscopic analysis of different clearing solutions. (a) SRS images of different clearing solutions at 2930 cm^{-1} and 2850 cm^{-1}. Scale bars: 20 μm. (b) SRS spectra of clearing solutions in the region from 2800 cm^{-1} to 3050 cm^{-1}. (c) Raman spectra taken by spontaneous Raman spectroscopy with 532 nm as excitation light.

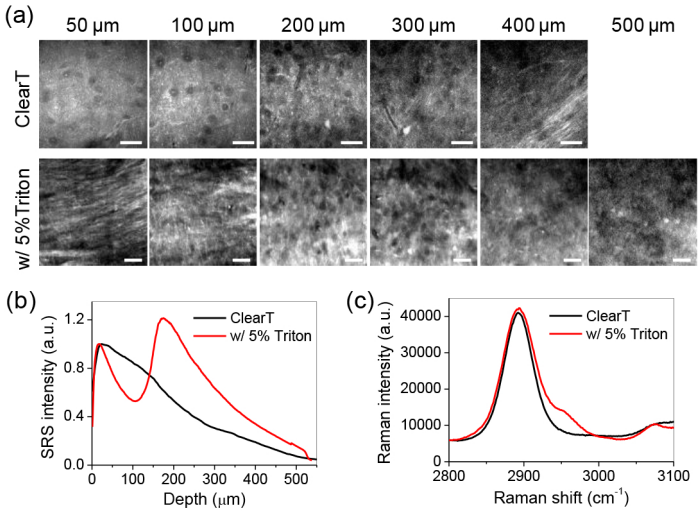

Fig. 4. Improvement of imaging depth with detergent. (a) SRS images taken at 2930 cm^{-1} from brain slices (~1 mm thick) cleared by ClearT solution with or without 5% Triton X-100 at indicated depth (see Visualization 8–Visualization 10). Individual neural cell bodies and nerve fiber can be resolved at indicated depths of brain slices. Two cortex layers (stronger signal) are reveled in the ClearT + 5% Triton X-100 cleared brain slice. Image display ranges were adjusted individually to better show the contrast. Scale bars: 20 μm. (b) Intensity profile over depth from the images shown in (a). (c) Raman spectra of ClearT solution with or without 5% Triton X-100.

Biomedical Optics EXPRESS

long time to scan the spectrum. To create the contrast needed for histopathology, we used two-color SRS microscopy at 2850 cm^{-1} and 2930 cm^{-1}, which correspond to CH_2 and CH_3 vibration, respectively.

To test whether this method works for cleared tissues, we applied hyperspectral SRS imaging in the region from ~2800 cm^{-1} to ~3050 cm^{-1} to cleared brain tissue slice (Visualization 11). SRS images at 2850 cm^{-1} (CH_3) and 2930 cm^{-1} (CH_2) show clear contrast between cells and background, because of much lower signal from clearing solution at these frequencies (Fig. 5(a)). Subtracting CH_2 image from CH_3 images results in an image with minimal background signal and highlighted nucleus areas. Composite of CH_2 image with the $CH_3 - CH_2$ image shows much improved contrast of nucleus and cytoplasm, generating a histology-like image with nucleus and cytoplasm highlighted in two pseudo colors (Fig. 5(a)). Using a lab-built LabView program, we acquired SRS images at these two Raman shifts at different depths with a step interval of 1 μm in depth. A 3D histological image was obtained (Fig. 5(b), Visualization 12). These data collectively demonstrate ClearT based tissue clearing enables SRS microscopy toward rapid 3D histopathology.

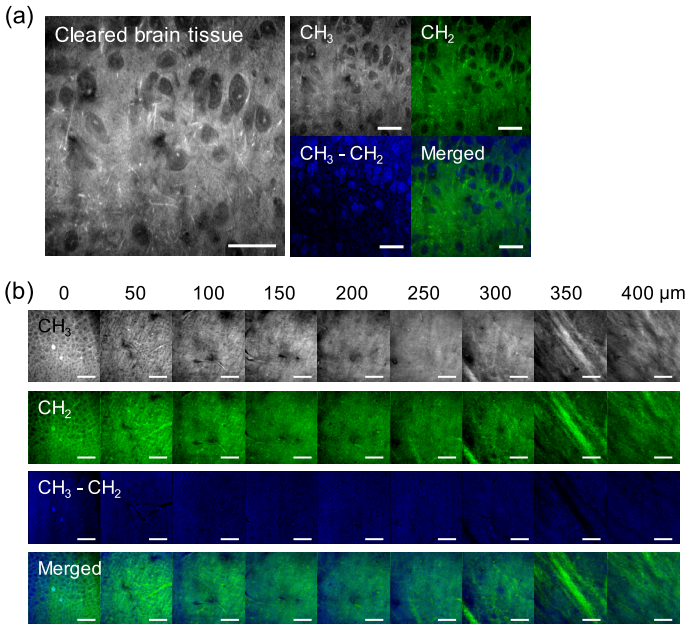

Fig. 5. Two-color SRS imaging of cleared tissue toward 3D histopathology. (a) Left: maximum intensity projection image projected from a hyperspectral SRS image stack of a brain tissue slice cleared with ClearT method with 5% Triton X-100 (see Visualization 11). Right: single frame SRS images at 2930 cm^{-1} (CH_3), 2850 cm^{-1} (CH_2), subtracted image ($CH_3 - CH_2$), and composite image of ($CH_3 - CH_2$) and (CH_2). Individual neural cell bodies are clearly resolved. (b) CH_3, CH_2, $CH_3 - CH_2$, and composite images of cleared brain slice at different depth (see Visualization 12). Neural cell bodies and nerve fibers are resolved at different layers of brain cortex. Image display ranges were adjusted individually to better show the contrast. Scale bars: 20 μm.

4. Discussion and outlooks

SRS histopathology avoids the need for staining with dyes by detecting intrinsic chemical bond vibrations. Chemical selectivity enables SRS microscopy to provide histology-like images, which lowers the barriers that hinder pathologists from adopting new techniques. Coupling tissue

Biomedical Optics EXPRESS

clearance, imaging depth of SRS microscopy is improved up to 500 μm, ~10-fold enhancement compared to imaging of uncleared tissues, allowing imaging of 1 mm thick tissue slices each time. Clearing of 1 mm thick slices only takes ~30 min, which is much faster than commonly used clearing method in fluorescence imaging, such as CUBIC or CLARITY [32]. It becomes more feasible to image the whole volume of a centimeter-size tissue block by sectioning it into a few 1 mm thick slices, instead of thousands of 5 μm thin slices. Through optical sectioning, it saves the time and efforts on imaging, registering and 3D reconstructing of individual 2D images, and minimizes image distortion caused by loss of individual slices or variation in staining intensity among individual slices. Therefore, 3D SRS histopathology holds the promise to improve the accuracy and efficiency of clinical pathological diagnosis.

Besides histopathology, 3D SRS microscopy is a powerful tool in deciphering the cell-to-cell heterogeneity in complex tissue environment. For example, cancer tissues have been known to exhibit intra-tumor heterogeneity [34,35]. There is an urgent demand for single-cell analysis tools to reveal the morphological, genomic and metabolic information of individual cells. SRS microscopy has the capability to reveal the morphological and metabolic information at single cell resolution. Brain tissues, as another example, have irregular organization and long-extending neuron cells. Elucidating the neural connection network relies on imaging with single-cell resolution in their 3D context. 3D SRS imaging has the potential to profile a large number of cells in tissues in their native organization at single cell level.

In this study, we find ClearT method clears the tissues much faster (~30 min) than other small molecule aqueous solution based methods, which usually take days to weeks. The key molecule in ClearT solution is formamide. Compared to urea or other sugar molecules, such as sucrose or fructose, the molecular size of formamide is smaller and it is miscible with water. Therefore, it might diffuse deeper and faster than urea or sucrose. With our current imaging set up, the maximal depth we can achieve with discernable image quality is ~500 μm. The penetration depth could be further improved with higher excitation power, which is limited by the laser source in our current set up. Using an objective with higher N.A. and long working distance (> 1 mm) could further improve the focus of light in deep tissue and increase the imaging depth. As SRS microscopy uses two laser beams (pump beam at 798 nm and Stokes beam at 1040 nm), chromatic aberrations between two beams might increase with depth. Through adaptive optics to correct the aberrations, one can potentially improve the spatial overlap between two beams at deep tissue level and consequently increase the imaging depth further.

Funding

National Institutes of Health (NIH) (R33CA223581, R01CA224275); National Science Foundation (NSF) (CHE1807106).

Acknowledgements

The authors acknowledge Dr. Chien-Sheng Liao for initial system setup and optimization.

Disclosures

The authors declare that there are no conflicts of interest related to this article.

References

1. E. Provenzano, V. Bossuyt, G. Viale, D. Cameron, S. Badve, C. Denkert, G. MacGrogan, F. Penault-Llorca, J. Boughey, G. Curigliano, J. M. Dixon, L. Esserman, G. Fastner, T. Kuehn, F. Peintinger, G. von Minckwitz, J. White, W. Yang, and W. F. Symmans, "Standardization of pathologic evaluation and reporting of postneoadjuvant specimens in clinical trials of breast cancer: recommendations from an international working group," Mod. Pathol. **28**(9), 1185–1201 (2015).
2. N. Roberts, D. Magee, Y. Song, K. Brabazon, M. Shires, D. Crellin, N. M. Orsi, R. Quirke, P. Quirke, and D. Treanor, "Toward Routine Use of 3D Histopathology as a Research Tool," Am. J. Pathol. **180**(5), 1835–1842 (2012).

Biomedical Optics EXPRESS

3. R. M. Nolan, S. G. Adie, M. Marjanovic, E. J. Chaney, F. A. South, G. L. Monroy, N. D. Shemonski, S. J. Erickson-Bhatt, R. L. Shelton, A. J. Bower, D. G. Simpson, K. A. Cradock, Z. G. Liu, P. S. Ray, and S. A. Boppart, "Intraoperative optical coherence tomography for assessing human lymph nodes for metastatic cancer," BMC Cancer **16**(1), 144 (2016).
4. F. T. Nguyen, A. M. Zysk, E. J. Chaney, S. G. Adie, J. G. Kotynek, U. J. Oliphant, F. J. Bellafiore, K. M. Rowland, P. A. Johnson, and S. A. Boppart, "Optical Coherence Tomography: The Intraoperative Assessment of Lymph Nodes in Breast Cancer," IEEE Eng. Med. Biol. Mag. **29**(2), 63–70 (2010).
5. M. Pilling and P. Gardner, "Fundamental developments in infrared spectroscopic imaging for biomedical applications," Chem. Soc. Rev. **45**(7), 1935–1957 (2016).
6. C. Petibois and G. Déléris, "Chemical mapping of tumor progression by FT-IR imaging: towards molecular histopathology," Trends Biotechnol. **24**(10), 455–462 (2006).
7. D. C. Fernandez, R. Bhargava, S. M. Hewitt, and I. W. Levin, "Infrared spectroscopic imaging for histopathologic recognition," Nat. Biotechnol. **23**(4), 469–474 (2005).
8. S. Tiwari, J. Raman, V. Reddy, A. Ghetler, R. P. Tella, Y. Han, C. R. Moon, C. D. Hoke, and R. Bhargava, "Towards Translation of Discrete Frequency Infrared Spectroscopic Imaging for Digital Histopathology of Clinical Biopsy Samples," Anal. Chem. **88**(20), 10183–10190 (2016).
9. K. L. Andrew Chan and S. G. Kazarian, "Attenuated total reflection Fourier-transform infrared (ATR-FTIR) imaging of tissues and live cells," Chem. Soc. Rev. **45**(7), 1850–1864 (2016).
10. T. T. W. Wong, R. Zhang, P. Hai, C. Zhang, M. A. Pleitez, R. L. Aft, D. V. Novack, and L. V. Wang, "Fast label-free multilayered histology-like imaging of human breast cancer by photoacoustic microscopy," Sci. Adv. **3**(5), e1602168 (2017).
11. F. Fereidouni, Z. T. Harmany, M. Tian, A. Todd, J. A. Kintner, J. D. McPherson, A. D. Borowsky, J. Bishop, M. Lechpammer, S. G. Demos, and R. Levenson, "Microscopy with ultraviolet surface excitation for rapid slide-free histology," Nat. Biomed. Eng. **1**(12), 957–966 (2017).
12. A. K. Glaser, N. P. Reder, Y. Chen, E. F. McCarty, C. Yin, L. Wei, Y. Wang, L. D. True, and J. T. C. Liu, "Light-sheet microscopy for slide-free non-destructive pathology of large clinical specimens," Nat. Biomed. Eng. **1**(7), 0084 (2017).
13. M. Balu, G. Lentsch, D. Z. Korta, K. König, K. M. Kelly, B. J. Tromberg, and C. B. Zachary, "In vivo multiphoton-microscopy of picosecond-laser-induced optical breakdown in human skin," Lasers Surg. Med. **49**(6), 555–562 (2017).
14. M. Balu, H. Mikami, J. Hou, E. O. Potma, and B. J. Tromberg, "Rapid mesoscale multiphoton microscopy of human skin," Biomed. Opt. Express **7**(11), 4375–4387 (2016).
15. J. Popp, Optical biopsies using multimodal imaging - chances and limitations, in *Biophotonics Congress: Biomedical Optics Congress 2018 (Microscopy/Translational/Brain/OTS)*. 2018. Hollywood, Florida: Optical Society of America.
16. T. W. Bocklitz, F. S. Salah, N. Vogler, S. Heuke, O. Chernavskaia, C. Schmidt, M. J. Waldner, F. R. Greten, R. Bräuer, M. Schmitt, A. Stallmach, I. Petersen, and J. Popp, "Pseudo-HE images derived from CARS/TPEF/SHG multimodal imaging in combination with Raman-spectroscopy as a pathological screening tool," BMC Cancer **16**(1), 534 (2016).
17. Y. Sun, S. You, H. Tu, D. R. Spillman, E. J. Chaney, M. Marjanovic, J. Li, R. Barkalifa, J. Wang, A. M. Higham, N. N. Luckey, K. A. Cradock, Z. George Liu, and S. A. Boppart, "Intraoperative visualization of the tumor microenvironment and quantification of extracellular vesicles by label-free nonlinear imaging," Sci. Adv. **4**(12), eaau5603 (2018).
18. J.-X. Cheng and X. S. Xie, "Vibrational spectroscopic imaging of living systems: An emerging platform for biology and medicine," Science **350**(6264), aaa8870 (2015).
19. R. Mittal, M. Balu, T. Krasieva, E. O. Potma, L. Elkeeb, C. B. Zachary, and P. Wilder-Smith, "Evaluation of stimulated raman scattering microscopy for identifying squamous cell carcinoma in human skin," Lasers Surg. Med. **45**(8), 496–502 (2013).
20. F.-K. Lu, D. Calligaris, O. I. Olubiyi, I. Norton, W. Yang, S. Santagata, X. S. Xie, A. J. Golby, and N. Y. R. Agar, "Label-Free Neurosurgical Pathology with Stimulated Raman Imaging," Cancer Res. **76**(12), 3451–3462 (2016).
21. M. Ji, S. Lewis, S. Camelo-Piragua, S. H. Ramkissoon, M. Snuderl, S. Venneti, A. Fisher-Hubbard, M. Garrard, D. Fu, A. C. Wang, J. A. Heth, C. O. Maher, N. Sanai, T. D. Johnson, C. W. Freudiger, O. Sagher, X. S. Xie, and D. A. Orringer, "Detection of human brain tumor infiltration with quantitative stimulated Raman scattering microscopy," Sci. Transl. Med. **7**(309), 309ra163 (2015).
22. M. Ji, D. A. Orringer, C. W. Freudiger, S. Ramkissoon, X. Liu, D. Lau, A. J. Golby, I. Norton, M. Hayashi, N. Y. R. Agar, G. S. Young, C. Spino, S. Santagata, S. Camelo-Piragua, K. L. Ligon, O. Sagher, and X. S. Xie, "Rapid, Label-Free Detection of Brain Tumors with Stimulated Raman Scattering Microscopy," Sci. Transl. Med. **5**(201), 201ra119 (2013).
23. C. W. Freudiger, R. Pfannl, D. A. Orringer, B. G. Saar, M. Ji, Q. Zeng, L. Ottoboni, W. Ying, C. Waeber, J. R. Sims, P. L. De Jager, O. Sagher, M. A. Philbert, X. Xu, S. Kesari, X. S. Xie, and G. S. Young, "Multicolored stain-free histopathology with coherent Raman imaging," Lab. Invest. **92**(10), 1492–1502 (2012).
24. D. A. Orringer, B. Pandian, Y. S. Niknafs, T. C. Hollon, J. Boyle, S. Lewis, M. Garrard, S. L. Hervey-Jumper, H. J. L. Garton, C. O. Maher, J. A. Heth, O. Sagher, D. A. Wilkinson, M. Snuderl, S. Venneti, S. H. Ramkissoon, K. A. McFadden, A. Fisher-Hubbard, A. P. Lieberman, T. D. Johnson, X. S. Xie, J. K. Trautman, C. W. Freudiger, and S. Camelo-Piragua, "Rapid intraoperative histology of unprocessed surgical specimens via fibre-laser-based stimulated Raman scattering microscopy," Nat. Biomed. Eng. **1**(2), 0027 (2017).

Biomedical Optics EXPRESS

25. X. Chen, C. Zhang, P. Lin, K.-C. Huang, J. Liang, J. Tian, and J.-X. Cheng, "Volumetric chemical imaging by stimulated Raman projection microscopy and tomography," Nat. Commun. **8**(1), 15117 (2017).
26. M. Wei, L. Shi, Y. Shen, Z. Zhao, A. Guzman, L. J. Kaufman, L. Wei, and W. Min, "Volumetric chemical imaging by clearing-enhanced stimulated Raman scattering microscopy," Proc. Natl. Acad. Sci. U. S. A. **116**(14), 6608–6617 (2019).
27. B. Liu, H. J. Lee, D. Zhang, C.-S. Liao, N. Ji, Y. Xia, and J.-X. Cheng, "Label-free spectroscopic detection of membrane potential using stimulated Raman scattering," Appl. Phys. Lett. **106**(17), 173704 (2015).
28. D. Zhu, K. V. Larin, Q. Luo, and V. V. Tuchin, "Recent progress in tissue optical clearing," Laser Photonics Rev. **7**(5), 732–757 (2013).
29. T. Kuwajima, A. A. Sitko, P. Bhansali, C. Jurgens, W. Guido, and C. Mason, "ClearT: a detergent- and solvent-free clearing method for neuronal and non-neuronal tissue," Development **140**(6), 1364–1368 (2013).
30. H. Hama, H. Kurokawa, H. Kawano, R. Ando, T. Shimogori, H. Noda, K. Fukami, A. Sakaue-Sawano, and A. Miyawaki, "Scale: a chemical approach for fluorescence imaging and reconstruction of transparent mouse brain," Nat. Neurosci. **14**(11), 1481–1488 (2011).
31. P. S. Tsai, J. P. Kaufhold, P. Blinder, B. Friedman, P. J. Drew, H. J. Karten, P. D. Lyden, and D. Kleinfeld, "Correlations of Neuronal and Microvascular Densities in Murine Cortex Revealed by Direct Counting and Colocalization of Nuclei and Vessels," J. Neurosci. **29**(46), 14553–14570 (2009).
32. D. S. Richardson and J. W. Lichtman, "Clarifying Tissue Clearing," Cell **162**(2), 246–257 (2015).
33. D. Fu and X. S. Xie, "Reliable Cell Segmentation Based on Spectral Phasor Analysis of Hyperspectral Stimulated Raman Scattering Imaging Data," Anal. Chem. **86**(9), 4115–4119 (2014).
34. D. A. Lawson, K. Kessenbrock, R. T. Davis, N. Pervolarakis, and Z. Werb, "Tumour heterogeneity and metastasis at single-cell resolution," Nat. Cell Biol. **20**(12), 1349–1360 (2018).
35. I. Dagogo-Jack and A. T. Shaw, "Tumour heterogeneity and resistance to cancer therapies," Nat. Rev. Clin. Oncol. **15**(2), 81–94 (2018).